

Gapped out-of-phase plasmon modes in alternating-twist multilayer graphene

Taejun Kim and Hongki Min

Department of Physics and Astronomy, Seoul National University, Seoul 08826, Korea

(Dated: February 16, 2026)

We theoretically investigate the plasmon modes of alternating-twist multilayer graphene. In multilayer systems, interlayer coupling gives rise to distinctive plasmon modes, but calculations in moiré systems remain challenging due to their complex tunneling structures. Using the Kac-Murdock-Szegő Toeplitz formalism, we derive that the in-phase mode exhibits the conventional \sqrt{q} behavior, while the out-of-phase modes acquire plasmon gaps determined by specific interband transitions between Dirac cones with different velocities in the long-wavelength limit. We demonstrate that these out-of-phase modes remain undamped in the weak Coulomb-interaction limit when the twist angle exceeds a critical value ($\theta \gtrsim 2.75^\circ$ for the alternating-twist trilayer case), regardless of the carrier density as long as the low-energy effective Dirac Hamiltonian remains valid. Furthermore, we consider the effect of a perpendicular electric field, and demonstrate how plasmon modes can be tuned by a gate voltage.

I. INTRODUCTION

Twisted systems have been the focus of intense interest following the observation of superconductivity and correlated insulating phases in magic-angle twisted bilayer graphene (TBG) [1–4]. TBG consists of two graphene sheets separated by an interlayer distance of $d \approx 3 \text{ \AA}$ and rotated by a twist angle θ [5–11]. The resulting spatially varying interlayer coupling gives rise to a long-period moiré superlattice, which in turn produces interesting electronic properties that are strongly dependent on the twist angle. In particular, nearly flat bands emerge at the so-called magic angle $\theta \approx 1.1^\circ$ [12–15], providing an ideal platform to study correlated physics, where the suppression of kinetic energy due to band flattening enhances the role of electron-electron interactions.

In recent years, plasmon modes, which are collective charge oscillations, in TBG have attracted great attention, both theoretically and experimentally [16–22]. Experimentally, near-field microscopy and Fourier transform infrared spectroscopy have demonstrated the existence of new plasmon modes in TBG, including chiral and slow plasmons [21, 22]. Furthermore, owing to its moiré band structure and the layer degree of freedom, TBG is theoretically predicted to host an angle-tunable acoustic plasmon [23], thereby unveiling new electromagnetic dynamics and exemplifying it as a unique quantum-optical platform.

In this regard, beyond TBG, collective excitations in alternating-twist multilayer graphene (ATMG) present an intriguing problem. Theoretically, in decoupled N -layer systems, there is one in-phase mode with the conventional dispersion ($\omega \propto \sqrt{q}$) and $N - 1$ out-of-phase modes with linear dispersions ($\omega \propto q$) [24–27]. When isotropic interlayer tunneling is present, the out-of-phase modes develop plasmon gaps whereas the in-phase mode remains unaffected [27, 28]. However, the effects of interlayer tunneling in moiré systems on these out-of-phase modes remains an open question due to their complex structures.

In this paper, we theoretically analyze how interlayer

interactions in ATMG affect plasmon modes. Using the Coulomb-eigenvector basis, which can be obtained exactly from Kac-Murdock-Szegő (KMS) Toeplitz matrices [27, 29–33], we find that the in-phase mode exhibits the conventional \sqrt{q} dispersion, whereas the out-of-phase modes develop plasmon gaps governed by specific interband transitions between Dirac cones with different velocities. We also investigate the effect of a perpendicular electric field, which splits the Dirac nodes and yields gate-tunable plasmon gaps.

This paper is organized as follows. In Sec. II, we introduce the random phase approximation (RPA) for multilayer systems and the KMS Toeplitz formalism. In Sec. III, we approximately derive the plasmon modes from the low-energy effective Hamiltonian of ATMG in the long-wavelength limit and compare our theoretical results with full numerical calculations. Sec. IV addresses the role of an applied perpendicular electric field in ATMG. Finally, in Sec. V, we conclude with discussions on the effect of the number of layers, the dependence on the twist angle, and the validity of our model with respect to the electric field and carrier density.

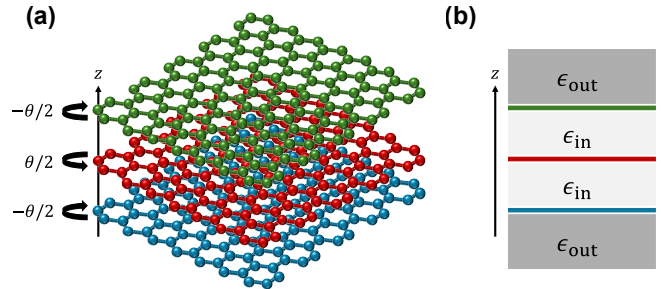


FIG. 1. Schematic illustrations of (a) the ATMG with $N = 3$ layers and (b) a front view of the ATMG embedded in a dielectric environment with dielectric constants ϵ_{in} (inside) and ϵ_{out} (outside). Here, z represents the out-of-plane direction.

II. RPA THEORY APPLIED TO MULTILAYER SYSTEMS

We consider a single-particle Hamiltonian $H(\mathbf{k})$ for an N -layer system with interlayer separation d , assuming that the material is embedded between two dielectric media of dielectric constant ϵ_{out} , while the space between the layers is filled with another dielectric medium of dielectric constant ϵ_{in} (see Fig. 1). The corresponding eigenstates are denoted by $|\mathbf{k}, \lambda\rangle$ with energy dispersions $\epsilon_{\mathbf{k}, \lambda}$ and the band index λ . Throughout this paper, we set $\hbar = 1$.

To describe the collective modes in multilayer systems, we consider the imaginary-time response function in the layer basis as [34–37]

$$\chi_{ij}^{(0)}(\mathbf{q}, i\Omega_m) = \frac{1}{\beta} \sum_{i\omega_n} \frac{g}{V} \sum_{\mathbf{k}} \text{tr}[G(\mathbf{k}, i\omega_n) P_i \times G(\mathbf{k} + \mathbf{q}, i\omega_n + i\Omega_m) P_j]. \quad (1)$$

Here, g is the spin-valley degeneracy, i, j are the layer indices, P_i is the projection operator on the i th layer, $\omega_n = (2n + 1)\pi/\beta$ and $\Omega_m = 2m\pi/\beta$ are the fermionic and bosonic Matsubara frequencies with $\beta = 1/k_B T$, where k_B denotes the Boltzmann constant and T is the temperature. The Green's function is defined as

$$G(\mathbf{k}, i\omega) = \frac{1}{i\omega - H(\mathbf{k})} = \sum_{\lambda} \frac{|\mathbf{k}, \lambda\rangle \langle \mathbf{k}, \lambda|}{i\omega - \epsilon_{\mathbf{k}, \lambda}}. \quad (2)$$

Performing the Matsubara frequency summation, and taking the analytic continuation $i\Omega_m \rightarrow \omega + i\eta$ (with η being a positive infinitesimal), we obtain the noninteracting density-density response function as

$$\chi_{ij}^{(0)}(\mathbf{q}, \omega) = \frac{g}{V} \sum_{\mathbf{k}, \lambda, \lambda'} \frac{f_{\mathbf{k}, \lambda} - f_{\mathbf{k} + \mathbf{q}, \lambda'}}{\omega + \epsilon_{\mathbf{k}, \lambda} - \epsilon_{\mathbf{k} + \mathbf{q}, \lambda'} + i\eta} \times F_{ij}^{\lambda\lambda'}(\mathbf{k}, \mathbf{k} + \mathbf{q}), \quad (3)$$

where $F_{ij}^{\lambda\lambda'}(\mathbf{k}, \mathbf{k}') = \langle \mathbf{k}, \lambda | P_i | \mathbf{k}', \lambda' \rangle \langle \mathbf{k}', \lambda' | P_j | \mathbf{k}, \lambda \rangle$ is the overlap factor and $f_{\mathbf{k}, \lambda} = [e^{\beta(\epsilon_{\mathbf{k}, \lambda} - \mu)} + 1]^{-1}$ is the Fermi-Dirac distribution at the chemical potential μ . We set $T = 0$ K in this paper, so that the Fermi distribution simplifies to a step function $f_{\mathbf{k}, \lambda} = \Theta(\mu - \epsilon_{\mathbf{k}, \lambda})$.

The matrix elements of the RPA dielectric function in the layer basis can be calculated as

$$\epsilon_{ij}(\mathbf{q}, \omega) = \delta_{ij} - \sum_k V_{ik}(q) \chi_{kj}^{(0)}(\mathbf{q}, \omega). \quad (4)$$

Here, the elements of the Coulomb matrix $V_{ij}(q)$ represent the Coulomb interactions between the i th and j th layers with $q = |\mathbf{q}|$. The bare Coulomb interactions, influenced by the dielectric environment, can be obtained from a straightforward electrostatics calculation [38]. We find that, in the long-wavelength limit, the Coulomb matrix eigenvalues $V_{\alpha}(q)$ and the corresponding eigenvectors

$\mathbf{u}_{\alpha}(q) = \frac{1}{N_{\alpha}} [u_{\alpha}^{(1)}(q), u_{\alpha}^{(2)}(q), \dots, u_{\alpha}^{(N)}(q)]^T$ with the normalization constant N_{α} ($\alpha = 1, 2, \dots, N$) take the form of those in a special case of a Toeplitz matrix known as the KMS matrix [27, 29–33]. By solving the KMS matrix, the Coulomb eigenvalues and eigenvectors in the long-wavelength limit are obtained as

$$V_{\alpha}(q \rightarrow 0) = \frac{2\pi e^2}{q} \times \begin{cases} \frac{N}{\epsilon_{\text{out}}}, & \alpha = 1, \\ \frac{1}{\epsilon_{\text{in}}} \frac{qd}{1 - \cos(\frac{\alpha-1}{N}\pi)}, & \alpha \neq 1, \end{cases} \quad (5a)$$

$$u_{\alpha}^{(k)}(q \rightarrow 0) = \cos \left[\frac{(2k-1)(\alpha-1)}{2N} \pi \right]. \quad (5b)$$

We leave the details in Appendix A. Note that the Coulomb eigenvalue of the in-phase mode ($\alpha = 1$) is governed primarily by the dielectric constant ϵ_{out} , while those of the out-of-phase modes ($\alpha \neq 1$) are governed by ϵ_{in} .

In the Coulomb eigenvector basis, the dielectric function can be expressed as [27]

$$\epsilon_{\alpha\beta}(\mathbf{q}, \omega) = \delta_{\alpha\beta} - V_{\alpha}(q) \chi_{\alpha\beta}^{(0)}(\mathbf{q}, \omega). \quad (6)$$

Here, $\chi_{\alpha\beta}^{(0)}(\mathbf{q}, \omega)$ denotes the noninteracting density-density response function in the Coulomb eigenvector basis. It can be obtained from Eq. (3) by replacing the overlap factor $F_{ij}^{\lambda\lambda'}(\mathbf{k}, \mathbf{k}')$ with $F_{\alpha\beta}^{\lambda\lambda'}(\mathbf{k}, \mathbf{k}') = \langle \mathbf{k}, \lambda | U_{\alpha} | \mathbf{k}', \lambda' \rangle \langle \mathbf{k}', \lambda' | U_{\beta} | \mathbf{k}, \lambda \rangle$, where $U_{\alpha} = \text{diag}[\mathbf{u}_{\alpha}(q) \otimes \mathbb{I}]$ with the identity matrix \mathbb{I} of the single layer. Note that the Coulomb eigenvectors alternate in parity: those with odd indices are symmetric with respect to the midpoint, while those with even indices are antisymmetric. Unlike the layer basis, which requires full matrix diagonalization, the Coulomb eigenbasis imposes strong selection rules for interband transitions that make analytical treatment more tractable. In particular, for systems whose bands are either symmetric or antisymmetric, interband transitions between symmetric and antisymmetric bands occur only via antisymmetric Coulomb modes, whereas all other transitions proceed through symmetric modes.

III. COLLECTIVE EXCITATIONS OF ATMG

A. Continuum model for ATMG

We consider a continuum Hamiltonian for an N -layer graphene system in the moiré Brillouin zone (mBZ), where the i th layer is twisted alternately by an angle $\theta_i = (-1)^i \theta/2$. The Hamiltonian of ATMG is given by [39–41]

$$H = \begin{pmatrix} h^{(1)}(\mathbf{k}) & T(\mathbf{r}) & 0 & \dots \\ T^{\dagger}(\mathbf{r}) & h^{(2)}(\mathbf{k}) & T^{\dagger}(\mathbf{r}) & \dots \\ 0 & T(\mathbf{r}) & h^{(3)}(\mathbf{k}) & \dots \\ \vdots & \vdots & \vdots & \ddots \end{pmatrix}, \quad (7)$$

where $h^{(i)}(\mathbf{k}) = v_0(\mathbf{k} \cdot \boldsymbol{\sigma}_{\theta_i})$, with $\boldsymbol{\sigma}_{\theta_i} = e^{\frac{i}{2}\theta_i\sigma_z}\boldsymbol{\sigma}e^{-\frac{i}{2}\theta_i\sigma_z}$, describes the Dirac cones of the twisted layers, and $T(\mathbf{r})$ denotes the interlayer tunneling. Here, $v_0 = \sqrt{3}|t|a/2$ is the Fermi velocity of monolayer graphene, with the nearest-neighbor hopping parameter $t = -3.1$ eV and lattice constant $a = 2.46$ Å. The corresponding interlayer hopping can be expressed as

$$T(\mathbf{r}) = \sum_{j=0,\pm} e^{i\mathbf{q}_j \cdot \mathbf{r}} T_j, \quad (8)$$

where $\mathbf{q}_{\pm} = 2k_D \sin(\theta/2)(\pm\sqrt{3}/2, 1/2)^T$ and $\mathbf{q}_0 = 2k_D \sin(\theta/2)(0, -1)^T$ represent three equivalent hopping paths between the adjacent layers with $k_D = 4\pi/3a$. Taking into account the lattice corrugation arising from out-of-plane relaxation [42–44], the interlayer tunneling matrices are written as

$$T_0 = \begin{pmatrix} w' & w \\ w & w' \end{pmatrix}, \quad T_{\pm} = \begin{pmatrix} w' & we^{\mp i\frac{2\pi}{3}} \\ we^{\pm i\frac{2\pi}{3}} & w' \end{pmatrix} \quad (9)$$

with the intrasublattice (intersublattice) hopping term given by $w' = 93.9$ meV ($w = 120$ meV). For the full numerical calculations, we consider the corrugated lattice structure with unequal hopping strengths ($w \neq w'$), whereas for the analytic calculation we adopt the rigid model with equal hopping terms ($w = w' = 120$ meV) [45].

The energy levels and corresponding wave functions of ATMG near the two mBZ corners \bar{K} and \bar{K}' can be obtained within the first-shell model, where the moiré reciprocal lattice vectors are truncated to the nearest reciprocal vectors and equal sublattice hopping terms ($w = w'$) are assumed. Near \bar{K} or \bar{K}' , the low-energy effective eigenfunctions of ATMG can be constructed following the solution of a one-dimensional chain problem as $|\Psi_{r,s}\rangle = \frac{1}{N_{\text{norm}}}(\Psi_{r,s}^{(1)}, \Psi_{r,s}^{(2)}, \dots, \Psi_{r,s}^{(N)})^T$ with the normalization constant N_{norm} , where [41]

$$\Psi_{r,s}^{(k)} = \sin(k\phi_r)\psi_{r,s}. \quad (10)$$

Here, $s = \pm 1$ indicates the band index of the Dirac cones, and $\phi_r = \frac{r\pi}{N+1}$ with $r = 1, 2, \dots, n$ for even $N = 2n$, or $r = 1, 2, \dots, n+1$ for odd $N = 2n+1$. Detailed expressions for $\psi_{r,s}$ are presented in Appendix B. The corresponding low-energy effective Hamiltonian of ATMG becomes $H_{\text{eff}} = v_r(\mathbf{k} \cdot \boldsymbol{\sigma})$, where the Fermi velocity v_r of the r th Dirac cone at \bar{K} or \bar{K}' is given by

$$\frac{v_r}{v_0} = \frac{1 - 12\tilde{\alpha}^2 \cos^2 \phi_r}{1 + 24\tilde{\alpha}^2 \cos^2 \phi_r} \quad (11)$$

with $\tilde{\alpha} = w/[2v_0k_D \sin(\theta/2)]$ denoting a dimensionless parameter. Note that the velocity of the r th Dirac cone is the same in each valley \bar{K} and \bar{K}' , and for an odd number of layers, the $(n+1)$ th mode near \bar{K} has a velocity $v_{n+1} = v_0$ equal to that of monolayer graphene.

The electronic bands of ATMG are either symmetric or antisymmetric with respect to the middle layer, as they

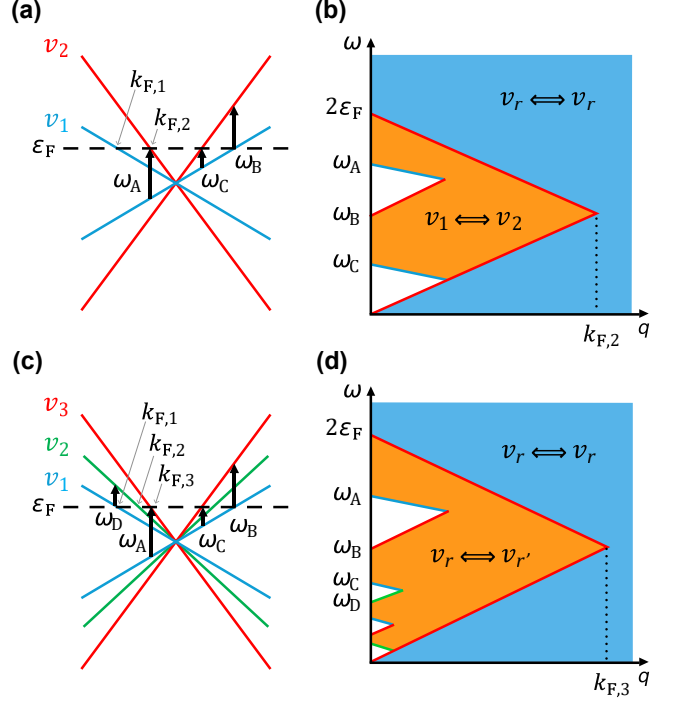


FIG. 2. Schematic illustrations of the band structures and associated particle-hole continua of ATMG. (a) Linear band dispersions for two Dirac cones with velocities v_1 and v_2 . Dashed black lines denote the Fermi energy ε_F and gray arrows represent the Fermi wave vector $k_{F,r}$. Black arrows depict representative interband transitions at $q = 0$ ($\omega_A - \omega_C$), given by $(v_1 + v_2)k_{F,2}$, $v_{21}k_{F,1}$, and $v_{21}k_{F,2}$, respectively. (b) The resulting particle-hole continuum in the (q, ω) plane for (a). The orange region indicates transitions between different Dirac cones, whereas the sky-blue regions denote transitions within the same Dirac cone. The boundaries are linear in $v_r q$, with slopes corresponding to the velocities indicated by the colors in (a). (c) Linear band dispersions for three Dirac cones with velocities v_1 , v_2 , and v_3 . Black arrows (labeled $\omega_A - \omega_D$) depict interband transitions given by $(v_1 + v_3)k_{F,3}$, $v_{31}k_{F,1}$, $v_{31}k_{F,3}$, and $v_{21}k_{F,1}$, respectively. (d) The resulting particle-hole continuum for (c), following the same color scheme as in (b).

originate from the solutions of a one-dimensional chain problem. Thus, one can use the symmetry properties of the Coulomb eigenbasis, which impose strong selection rules on interband transitions. In the presence of tunneling in ATMG, the plasmon modes derived from the low-energy effective Hamiltonian in the long-wavelength limit take the following form (see Appendix C):

$$\omega_1^2(q \rightarrow 0) = \frac{2\pi e^2}{\epsilon_{\text{out}}} \left(\sum_{\nu,r} \frac{n_{\nu,r}}{m_r} \right) q, \quad (12a)$$

$$\omega_{1<\alpha<\frac{N+2}{2}}^2(q \rightarrow 0) = \omega_{\text{gap},\alpha}^2 + C_{\alpha}q, \quad (12b)$$

where $n_{\nu,r}$ is the carrier (electron or hole) density of the r th Dirac cone at $\nu = \bar{K}$ or $\nu = \bar{K}'$, and $m_r = k_{F,r}/v_r$ is the effective mass defined using its Fermi wave vec-

tor $k_{F,r}$ with the Fermi energy $\varepsilon_F = v_r k_{F,r}$. Here, $\omega_{\text{gap},\alpha} = \omega_\alpha(q=0)$ is the gap of the out-of-phase mode with $\alpha = 2, \dots, \frac{N}{2}$ for even N or $\alpha = 2, \dots, \frac{N+1}{2}$ for odd N . Notably, these out-of-phase modes are governed by ϵ_{in} , whereas the in-phase mode ω_1 depends on ϵ_{out} . Approximately, the gap of the out-of-phase mode in the weak Coulomb-interaction limit can be expressed as

$$\omega_{\text{gap},\alpha} \approx v_{\alpha 1} k_{F,1} \quad (13)$$

with $v_{\alpha 1} = v_\alpha - v_1$. Here, $v_{\alpha 1} k_{F,1}$ corresponds to the transition energy labeled ω_B in Fig. 2. Unlike the case of isotropic tunneling, which yields one in-phase mode and $N-1$ out-of-phase modes, the above expressions do not capture all Coulomb eigenmodes. Within the scope of the low-energy theory, particularly where the Fermi energy crosses the Dirac cones, the plasmon modes ($\alpha \geq (N+2)/2$) are strongly suppressed, similar to those in AB bilayer and ABA trilayer graphene [46, 47].

To examine the conditions for Landau damping of out-of-phase plasmon modes, we need to consider the particle-hole continuum of the ATMG. In contrast to monolayer graphene, the presence of distinct velocities v_r allows for interband transitions between different Dirac cones. These transitions form a unique particle-hole continuum in the (q, ω) plane as shown in Fig. 2, which constrains the conditions for the formation of long-lived out-of-phase plasmons. Specifically, in the presence of Dirac cones with velocities v_1 and v_2 , the upper boundary of the particle-hole continuum at $q=0$ is given by $\omega_A = (v_1 + v_2)k_{F,2}$ in Fig. 2(a), in contrast to the conventional $2\varepsilon_F$ observed in monolayer graphene. Furthermore, interband transitions between the v_1 and v_2 Dirac cones give rise to a new particle-hole continuum in the range $\omega_C < \omega < \omega_B$ at $q=0$, where $\omega_B = v_{21}k_{F,1}$ and $\omega_C = v_{21}k_{F,2}$.

Based on Eq. (13) and the particle-hole continuum, we can identify the regime where the out-of-phase mode ω_α ($1 < \alpha < \frac{N+2}{2}$) becomes Landau damped. In the weak Coulomb-interaction limit, the out-of-phase mode ω_α with the largest index α remains undamped as long as $\omega_{\text{gap},\alpha} < \omega_A$, where $\omega_A = (v_1 + v_\alpha)k_{F,\alpha}$. In this case, from $\frac{v_\alpha}{v_1} - \frac{v_1}{v_\alpha} < 2$, we obtain $v_\alpha < (1 + \sqrt{2})v_1$, which is possible in the high-angle regime and implies that the out-of-phase mode remains undamped once the twist angle exceeds the critical θ_c regardless of the total carrier density n_{tot} . Analogously, we can determine the critical angles for the remaining out-of-phase modes, which are also independent of n_{tot} . For instance, the condition for the highest out-of-phase mode to be undamped is always satisfied whenever $\theta > \theta_c$ given in Table I, as long as the low-energy effective Dirac Hamiltonian remains valid. Furthermore, for $N=5$ or $N=6$, we find that the out-of-phase mode ω_2 is undamped when $\omega_D < \omega_C$, where $\omega_C = v_{31}k_{F,3}$ and $\omega_D = v_{21}k_{F,1}$, leading to the inequality $\frac{v_2}{v_1} + \frac{v_1}{v_3} < 2$. Similarly, we can identify the corresponding critical angle θ_c above which the mode ω_2 is undamped regardless of n_{tot} in the weak Coulomb-interaction limit. Although the actual plasmon gap is

TABLE I. Summary of the critical angles above which the out-of-phase plasmon modes are undamped in the weak Coulomb-interaction limit. Schematic figures show the dominant interband transitions for ω_α (black arrows) and the Fermi energy ε_F (dashed lines) at \bar{K} and \bar{K}' in the long-wavelength limit for a given N in ATMG. For $N=3$ and $N=4$, the critical angle for ω_2 is determined by the condition $v_2 = (1 + \sqrt{2})v_1$. For $N=5$ and $N=6$, θ_c is defined by $v_3 = (1 + \sqrt{2})v_1$ for ω_3 , and by $\frac{v_2}{v_1} + \frac{v_1}{v_3} = 2$ for ω_2 .

N	near \bar{K}	near \bar{K}'	θ_c
3			$\omega_2: 2.75^\circ$
4			$\omega_2: 2.93^\circ$
5			$\omega_2: 4.47^\circ$ $\omega_3: 3.37^\circ$
6			$\omega_2: 3.65^\circ$ $\omega_3: 3.41^\circ$

shifted by the Coulomb interaction, our findings indicate that the density-independence of the damping conditions is a robust feature of ATMG.

For numerical calculations, we consider the loss function of ATMG defined as [23, 27]

$$L(\mathbf{q}, \omega) = -\text{Im}\{\text{tr}[\epsilon^{-1}(\mathbf{q}, \omega)]\}, \quad (14)$$

which is related to the dynamical structure factor $S(\mathbf{q}, \omega) \propto L(\mathbf{q}, \omega)$, representing the spectral weight of electronic excitations. Throughout the main text, we choose \mathbf{q} along the $\bar{\Gamma} - \bar{M}$ direction, and results along the $\bar{\Gamma} - \bar{K}$ direction are presented in Appendix D. Collective excitations appear as sharp peaks in the loss function, arising from the roots of the equation $\det[\epsilon(\mathbf{q}, \omega)] = 0$. All calculations are carried out at a distance $d = 3$ Å and $T = 0$ K, using a finite broadening parameter $\eta = 1$ meV and dielectric constants $\epsilon_{\text{out}} = 5$ and $\epsilon_{\text{in}} = 1$. In

the following, we present the results for the cases $N = 3$ and $N = 4$, and leave the discussion of the $N = 5$ case to Sec. V.

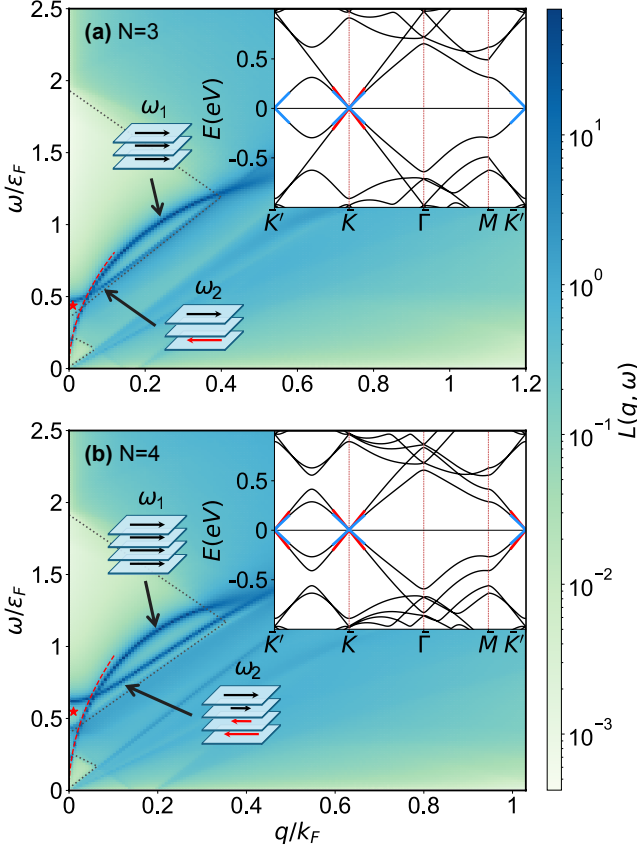


FIG. 3. Loss function $L(\mathbf{q}, \omega)$ of unbiased ATMG systems at a twist angle $\theta = 5^\circ$ with $\varepsilon_F = 0.2$ eV for (a) $N = 3$ ($n_{\text{tot}} = 1.3 \times 10^{13} \text{ cm}^{-2}$) and (b) $N = 4$ ($n_{\text{tot}} = 1.8 \times 10^{13} \text{ cm}^{-2}$). The insets show the band structures of ATMG, where the colored lines highlight the low-energy effective Dirac cones near \bar{K} and \bar{K}' . Coulomb eigenvectors of the in-phase and out-of-phase modes are illustrated. The red dashed lines indicate the analytically calculated in-plane plasmon dispersions, and the red stars mark the approximately obtained out-of-phase plasmon gaps using Eq. (15) for $N = 3$ and Eq. (16) for $N = 4$. The dotted gray lines represent the boundaries of the particle-hole continuum.

B. $N = 3$ case

Here, we present our calculations for alternating-twist trilayer graphene (AT3G). In the long-wavelength limit, the system exhibits two symmetric oscillation modes $[\mathbf{u}_1 \parallel (1, 1, 1)^T$ and $\mathbf{u}_3 \parallel (1, -1, -1)^T]$ and one antisymmetric oscillation mode $[\mathbf{u}_2 \parallel (1, 0, -1)^T]$. Figure 3(a) shows that there are two Dirac cones near \bar{K} : one with velocity $v_2 = v_0$ and an antisymmetric eigenvector, and the other with v_1 and a symmetric eigenvector, whereas

near \bar{K}' , there is a single Dirac cone with velocity v_1 and a symmetric eigenvector.

The numerical results for the plasmon modes are obtained from Eq. (14) at the twist angle $\theta = 5^\circ$. The in-phase mode (\mathbf{u}_1) arises from intraband transitions within Dirac cones in the mBZ and exhibits a \sqrt{q} dispersion given by Eq. (12a). The out-of-phase mode ω_2 arises from interband transitions between the v_1 and $v_2 = v_0$ Dirac cones at the \bar{K} point, which involve symmetric and antisymmetric bands. Then, we can approximately obtain the plasmon gap $\omega_{\text{gap},2}$ for the low-energy effective Hamiltonian from the solution of the equation as

$$\omega_{\text{gap},2} = v_{21}k_{F,1} + \delta\omega_2^{(3)}(\omega_{\text{gap},2}). \quad (15)$$

Here, the additional term $\delta\omega_2^{(3)}$ represents the Coulomb-interaction correction to the out-of-phase mode and is a function of $\omega_{\text{gap},2}$. See Appendix C for the detailed derivation and the definition of $\delta\omega_2^{(3)}$. Note that the in-phase mode ω_1 is symmetric, and thus only symmetric-symmetric or antisymmetric-antisymmetric bands contribute to the oscillation, while the out-of-phase mode ω_2 is antisymmetric, permitting only symmetric-antisymmetric bands to contribute to the oscillation. Since they originate from different types of Coulomb modes, they cannot couple to each other.

C. $N = 4$ case

In the case of alternating-twist tetralayer graphene (AT4G), we have two symmetric oscillation modes $[\mathbf{u}_1 \parallel (1, 1, 1, 1)^T$ and $\mathbf{u}_3 \parallel (1, -1, -1, 1)^T]$ and two antisymmetric oscillation modes $[\mathbf{u}_2 \parallel (1 + \sqrt{2}, \sqrt{2}, -\sqrt{2}, -1 - \sqrt{2})^T$ and $\mathbf{u}_4 \parallel (\sqrt{2} - 1, -1, 1, 1 - \sqrt{2})^T]$. At \bar{K} and \bar{K}' , there are two Dirac cones with velocities v_1 and v_2 as illustrated in Fig. 3(b). Similar to the AT3G case, the eigenvectors of the v_1 Dirac cones are symmetric, while the eigenvectors of the v_2 Dirac cones exhibit antisymmetric behavior near both \bar{K} and \bar{K}' .

Unlike AT3G, there are two Dirac cones at \bar{K}' in AT4G, and v_2 differs from v_0 . While these features lead to quantitative differences, the in-phase and out-of-phase modes stem from the same underlying mechanism as in AT3G. The in-phase mode (\mathbf{u}_1) arises from intraband transitions within the Dirac cones and exhibits a \sqrt{q} dispersion. The out-of-phase mode ω_2 arises from interband transitions between the v_1 and v_2 Dirac cones at both the \bar{K} and \bar{K}' points. The plasmon gap $\omega_{\text{gap},2}$ for the low-energy effective Hamiltonian can be obtained approximately from the solution of the equation as

$$\omega_{\text{gap},2} = v_{21}k_{F,1} + \delta\omega_2^{(4)}(\omega_{\text{gap},2}). \quad (16)$$

See Appendix C for the definition of $\delta\omega_2^{(4)}$. Just as in the AT3G case, the symmetric mode ω_1 cannot couple to the antisymmetric mode ω_2 .

IV. EFFECT OF A PERPENDICULAR ELECTRIC FIELD

In this section, we consider the plasmon modes of ATMG under a perpendicular electric field. In the presence of an interlayer potential difference U , we add a diagonal matrix $H_U = \text{diag}[U^{(1)}\mathbb{I}_2, U^{(2)}\mathbb{I}_2, \dots, U^{(N)}\mathbb{I}_2]$ to the Hamiltonian of ATMG in Eq. (7), where $U^{(i)}$ is defined to satisfy both $U^{(i+1)} - U^{(i)} = U$ and $U^{(1)} = -U^{(N)}$. Then, the low-energy effective Hamiltonian of each Dirac cone can be obtained from perturbation theory as [41]

$$H_{\text{eff}} = \Delta(\tilde{\alpha}) + \tilde{v}(\mathbf{k} \cdot \boldsymbol{\sigma}), \quad (17)$$

where $\Delta(\tilde{\alpha})$ is the energy shift due to the potential difference U and \tilde{v} is the modified Fermi velocity of the Dirac cone. The gapped out-of-phase mode is generated from interband transitions between the shifted Dirac cones. As in AA-stacked graphene, an undamped out-of-phase plasmon appears when the chemical potential exceeds the energy level associated with the maximum shift of the Dirac cone [48]. For $N = 4$, the shifts at \bar{K} and \bar{K}' occur in opposite directions, which makes Landau damping occur more easily for the out-of-phase mode. Furthermore, for larger N the increasing maximum shift hinders the formation of undamped out-of-phase modes [41]. We therefore restrict our analysis to the $N = 3$ case.

At \bar{K} , the effective Hamiltonian of AT3G in the presence of an interlayer potential U can be described as two Dirac cones with velocity $\tilde{v} = \frac{v_1+v_2}{2}$, split in energy by $\Delta_{\pm}(\tilde{\alpha}) = \pm C(\tilde{\alpha})U$ with $C(\tilde{\alpha}) = \frac{1}{\sqrt{1+12\tilde{\alpha}^2}}$, whereas the effective Hamiltonian at \bar{K}' remains unchanged by U [41]. Figure 4 shows that the in-phase mode is generated from the two shifted Dirac cones at \bar{K} and one Dirac cone at \bar{K}' , and it still exhibits a \sqrt{q} dispersion. For the gapped out-of-phase mode, which arises from interband transitions between the shifted Dirac cones, the gap $\omega_{\text{gap},2}$ can be roughly approximated as

$$\omega_{\text{gap},2} \approx 2C(\tilde{\alpha})U. \quad (18)$$

Note that the perturbation U mixes the eigenvectors of the one-dimensional chain model, so the selection rules for the Coulomb eigenvectors may no longer be applicable. Indeed, as U increases, the out-of-phase plasmon gap approaches the interband transition energy because U suppresses the Coulomb-interaction-induced shift of the plasmon gap (see Appendix E). Furthermore, at larger U , the mode eventually becomes Landau damped, no longer satisfying $\omega_{\text{gap},2} < 2\varepsilon_F$ as in AA-stacked graphene. Nevertheless, the out-of-phase mode still arises from the interband transitions between the two Dirac cones, indicating that the gap can be tuned by an applied gate electric field.

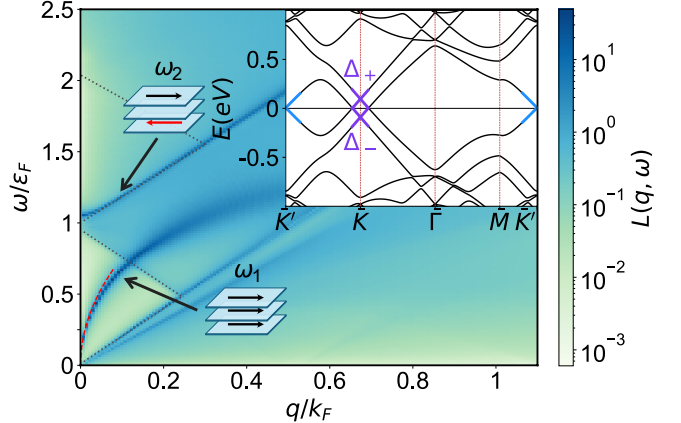


FIG. 4. Loss function $L(\mathbf{q}, \omega)$ of a biased AT3G system at a twist angle $\theta = 5^\circ$ under a perpendicular electric field $U = 0.1$ eV with $\varepsilon_F = 0.2$ eV ($n_{\text{tot}} = 1.5 \times 10^{13} \text{ cm}^{-2}$). The inset shows the band structure of a biased AT3G, where the colored lines highlight the perturbative Hamiltonian with energy splitting Δ_{\pm} near \bar{K} and \bar{K}' .

V. DISCUSSION

The analytically derived out-of-phase plasmon gaps [Eqs. (15) and (16)] for the effective Hamiltonian were obtained using the first-shell model, which employs nearest-neighbor truncation. When the twist angle decreases, the first-shell model is insufficient to accurately capture the band structure of the enlarged ATMG moiré superlattice, leading to discrepancies with the numerical results. In addition, as the carrier density increases, the low-energy effective Hamiltonian becomes less accurate at the Fermi level, so the approximately obtained plasmon gaps deviate from the numerical results. Nevertheless, our analytical analysis captures the out-of-phase plasmon mode in ATMG quite well in the large-twist-angle regime, consistent with full numerical calculations.

The present results focus on AT3G and AT4G. For the $N = 5$ case, three Dirac cones labeled by v_1, v_2 , and $v_3 = v_0$ exist near \bar{K} and two Dirac cones labeled by v_1 and v_2 exist near \bar{K}' as shown in Fig. 5. In contrast to the $N = 3$ and $N = 4$ cases, additional interband transitions between Dirac cones at \bar{K} emerge, giving rise to the out-of-phase mode ω_3 along with the out-of-phase mode ω_2 . As in the analysis above, intraband transitions generate the in-phase mode ω_1 , interband transitions between v_1 and v_2 and between v_2 and $v_3 = v_0$ generate the out-of-phase mode ω_2 , and interband transitions between v_1 and $v_3 = v_0$ generate the out-of-phase mode ω_3 . Note that the plasmon gaps exhibit the behavior $\omega_{\text{gap},\alpha} \approx v_{\alpha 1} k_{F,1}$ in the weak Coulomb-interaction limit, which suggests that a larger interband transition scale $v_{\alpha 1} k_{F,1}$ leads to a larger plasmon gap. However, the numerical results show that $\omega_{\text{gap},2}$ is larger than $\omega_{\text{gap},3}$. This difference arises because ω_2 is generated by multiple interband transitions at \bar{K} and \bar{K}' , whereas ω_3 is gener-

ated by a single interband transition at \bar{K} . As a result, the additional Coulomb-interaction contribution [see the additional term in Eq. (15) for the $N = 3$ case] becomes dominant for ω_2 , yielding a higher plasmon gap than that of ω_3 .

In our calculations, we focus on representative twist angles in the range $5^\circ - 7^\circ$, which lie above the typical magic-angle regime of $1^\circ - 2^\circ$. Since the Dirac velocity decreases as the angle becomes smaller, the inequality $v_\alpha < (1 + \sqrt{2})v_1$ with the largest Dirac velocity v_α is no longer satisfied below a certain angle, and the out-of-phase mode becomes Landau damped. Figure 6(a) shows $\omega_{\text{gap},2}$ of an unbiased AT3G as a function of θ and n_{tot} . As expected, an undamped gapped out-of-phase mode appears only for angles above $\theta_c = 2.75^\circ$, but the numerical results exhibit some deviations from the analytic prediction obtained from the low-energy effective Dirac Hamiltonian. At low angles, the density range where the low-energy effective model remains valid shrinks, and the damping region for ω_2 expands with increasing density. At low densities, ω_2 is damped due to the use of a finite broadening parameter η rather than an infinitesimal one.

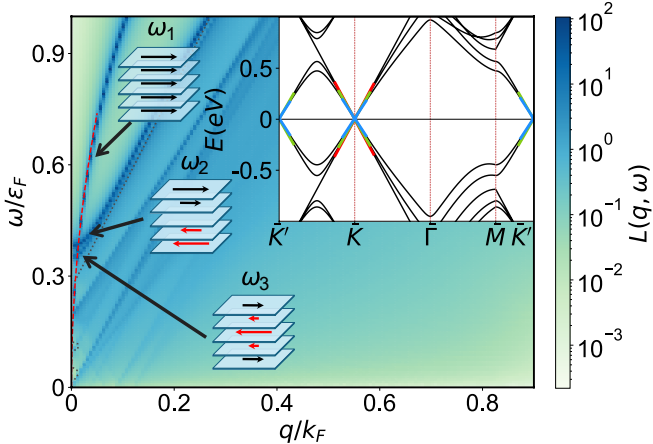


FIG. 5. Loss function $L(\mathbf{q}, \omega)$ of an unbiased AT5G system at a twist angle $\theta = 7^\circ$ with $\epsilon_F = 0.3$ eV ($n_{\text{tot}} = 4.1 \times 10^{13}$ cm $^{-2}$).

In the presence of a perpendicular electric field, the analytic form of the effective perturbative Hamiltonian in Eq. (17) is valid within a radius of about $k_c \sim U/v_0$ in momentum space. This implies that varying the total carrier density n_{tot} and the interlayer potential difference U modifies the out-of-phase mode, and the previously derived approximate expression for the out-of-phase plasmon gap in Eq. (17) no longer holds when the carrier density is large. Figure 6(b) illustrates $\omega_{\text{gap},2}$ in AT3G as a function of U and n_{tot} at $\theta = 5^\circ$. The result demonstrates that the out-of-phase mode is undamped if the potential difference U satisfies $2C(\tilde{\alpha})U < 2\epsilon_F$ in the weak Coulomb-interaction limit. We analytically obtain the critical density using U_c which corresponds to the black dashed line in Fig. 6(b). As in Fig. 6(a), the numerical results exhibit deviations arising from a finite broadening

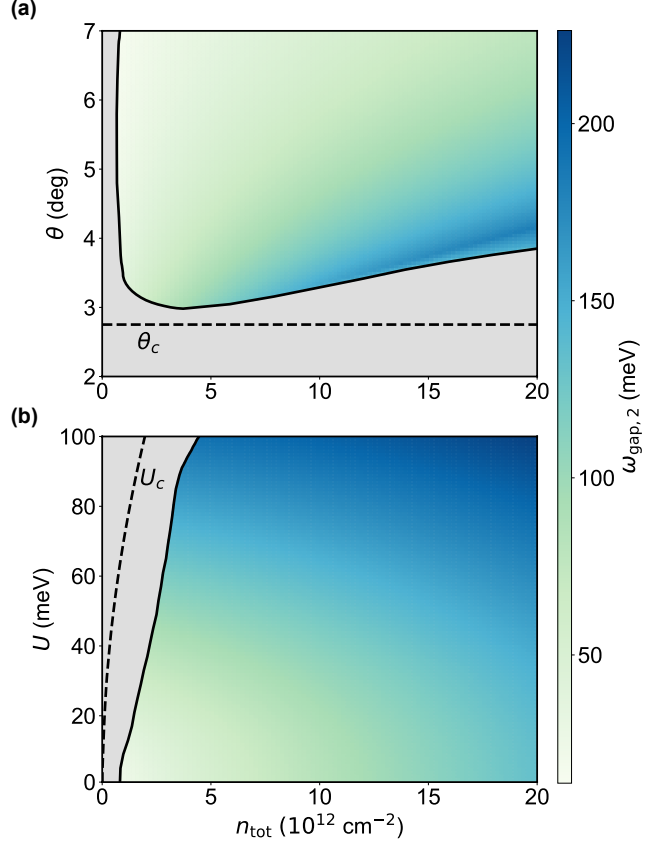


FIG. 6. The out-of-phase plasmon gap $\omega_{\text{gap},2}$ of an AT3G system is plotted as a function of (a) θ and n_{tot} with $U = 0$ eV and (b) U and n_{tot} for an angle $\theta = 5^\circ$. The black solid lines indicate the numerically determined boundaries where the plasmon is undamped. The black dashed lines represent the analytically obtained critical lines, using θ_c from $v_\alpha = (1 + \sqrt{2})v_1$ with the largest Dirac velocity v_α in (a) and U_c from $U = \epsilon_F/C(\tilde{\alpha})$ in (b), respectively.

parameter η at low densities and from the validity of the first-order correction in U at high densities.

We point out that ATMG provides a robust and versatile multilayer-graphene platform for engineering an undamped gapped out-of-phase plasmon mode at experimentally reasonable carrier densities. In contrast to AA-stacked (AB-stacked) bilayer graphene, where accessing an undamped gapped out-of-phase mode typically requires the Fermi energy $\epsilon_F \gtrsim t_\perp$ ($\epsilon_F \gtrsim t_\perp/2$) with the interlayer tunneling t_\perp [46, 48], corresponding to a high carrier density $n_{\text{tot}} \sim 10^{13}$ cm $^{-2}$, the out-of-phase mode in ATMG, in principle, remains undamped regardless of n_{tot} in the large-twist-angle regime. Moreover, the plasmon spectrum in ATMG is highly tunable through the twist angle, carrier doping, and an external electric field.

In summary, we have investigated plasmons in ATMG both analytically and numerically. Using a continuum Hamiltonian, we obtained numerical results for the plasmon modes, whereas using the low-energy effective Hamiltonian and the Coulomb eigenvector basis, we ob-

tained the corresponding analytical results. The in-phase mode exhibits a square-root dispersion of the form $\sqrt{q/\epsilon_{\text{out}}}$ with the dielectric constant ϵ_{out} , while the out-of-phase plasmon modes develop gaps governed by specific interband transitions between Dirac cones with the dielectric constant ϵ_{in} . We also demonstrated that, in the weak Coulomb-interaction limit, these out-of-phase modes are undamped when the twist angle is above the critical value, regardless of the density as long as the low-energy effective Dirac Hamiltonian remains valid. Furthermore, we found that the gap of the out-of-phase mode can be tuned by applying a perpendicular electric field, which shifts the Dirac cones and gives rise to plasmon features reminiscent of those observed in AA-stacked multilayer graphene. The analytic and numerical results for ATMG obtained here will help clarify the plasmonics of moiré systems.

ACKNOWLEDGMENTS

The work at SNU was supported by the National Research Foundation of Korea (NRF) grants funded by the Korea government (MSIT) (Grant No. RS-2023-NR076715), the Creative-Pioneering Researchers Program through Seoul National University (SNU), and the Center for Theoretical Physics.

Appendix A: Multilayer Coulomb interaction

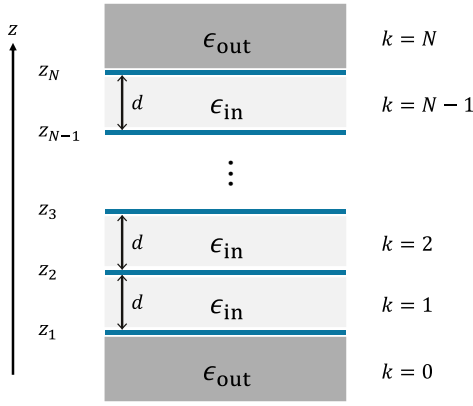


FIG. 7. Schematic illustration of the dielectric environment, consisting of N equally spaced sheets separated by a distance d . The system is characterized by dielectric constants ϵ_{in} (inside) and ϵ_{out} (outside). Here, z denotes the out-of-plane direction, where the sheet locations are given by $z_k = (k-1)d$ with $k = 1, 2, \dots, N$, and the regions are indexed by $k = 0, 1, \dots, N$.

We consider a system consisting of N equally spaced sheets separated by a distance d as shown in Fig. 7. The sheets are located at $z_k = (k-1)d$ with $k = 1, 2, \dots, N$.

The bare Coulomb matrix $V_{ij}(q)$ in the N -layer system can be determined by solving the Poisson equation [38]

$$\nabla \cdot [\epsilon(z) \nabla \phi(\rho, z)] = -4\pi\sigma_j, \quad (\text{A1})$$

where $\phi(\rho, z)$ denotes the electrostatic potential induced by a point charge $\sigma_j = (-e)\delta(\rho)\delta(z - z_j)$ in cylindrical coordinates. Here, the dielectric function is taken to be $\epsilon(z) = \epsilon_{\text{out}}$ for the outer regions ($z < z_1$ or $z > z_N$), and $\epsilon(z) = \epsilon_{\text{in}}$ for the inner regions ($z_k < z < z_{k+1}$). For convenience, we introduce an additional labeling such that the regions are indexed by $k = 0, 1, \dots, N$: regions $k = 0$ and $k = N$ correspond to the outer regions while $k = 1, 2, \dots, N-1$ denote the inner regions. The electric potential $\phi(\rho, z)$ can be defined piecewise in each of the $N+1$ regions. In the k th region, the electric potential takes the form

$$\phi(\rho, z) = \int \frac{d^2q}{(2\pi)^2} e^{i\mathbf{q}\cdot\mathbf{\rho}} (A_k e^{qz} + B_k e^{-qz}), \quad (\text{A2})$$

which involves a total of $2(N+1)$ constants A_k and B_k with the in-plane momentum \mathbf{q} and its magnitude $q = |\mathbf{q}|$. Note that the boundary conditions at infinity, $\phi(\rho, z \rightarrow \pm\infty) = 0$, impose $B_0 = 0$ and $A_N = 0$. The remaining $2N$ coefficients are determined by enforcing the continuity of the potential $\phi(\rho, z)$ and the discontinuity in the z component of the electric displacement $\mathbf{D}(\rho, z) = \epsilon(z)\mathbf{E}(\rho, z)$ with the electric field $\mathbf{E} = -\nabla\phi$.

After solving a routine electrostatic calculation, the Coulomb matrix $V_{ij}(q) = (-e)\tilde{\phi}(\mathbf{q}, z = z_i)$, where $\tilde{\phi}(\mathbf{q}, z)$ denotes the 2D Fourier transform of the electric potential induced by σ_j , can be obtained as

$$V_{ij}(q) = \frac{2\pi e^2}{\epsilon_{\text{in}} q} \frac{1}{f(q)} [\epsilon_+^2 e^{x_{ij}qd} + \epsilon_-^2 e^{-x_{ij}qd} + 2\epsilon_+ \epsilon_- \cosh(y_{ij}qd)], \quad (\text{A3})$$

where $f(q) = \epsilon_+^2 e^{q(N-1)d} - \epsilon_-^2 e^{-q(N-1)d}$ with $\epsilon_{\pm} = \epsilon_{\text{in}} \pm \epsilon_{\text{out}}$. Here, we define $x_{ij} = N - |i - j| - 1$ and $y_{ij} = N - i - j + 1$ for simplicity. If $\epsilon_{\text{in}} = \epsilon_{\text{out}}$, the interlayer Coulomb interaction reduces to a trivial form, $V_{ij} = \frac{2\pi e^2}{\epsilon_{\text{in}} q} e^{-q|i-j|d}$. In the long-wavelength limit ($q \rightarrow 0$), the Coulomb matrix in Eq. (A3) becomes

$$\begin{aligned} V_{ij}(q) &= \frac{8\pi e^2}{q} \frac{\epsilon_{\text{in}}}{f(q)} \left[1 + \frac{\epsilon_{\text{out}}}{\epsilon_{\text{in}}} x_{ij}qd + O(q^2) \right] \quad (\text{A4}) \\ &= \frac{8\pi e^2}{q} \frac{\epsilon_{\text{in}}}{f(q)} \left[\exp\left(\frac{\epsilon_{\text{out}}}{\epsilon_{\text{in}}} x_{ij}qd\right) + O(q^2) \right], \end{aligned}$$

where we use $\exp(x) \approx 1 + x$. Note that the Coulomb matrix in the long-wavelength limit is proportional to the KMS matrix $A_{ij}(\rho) = \rho^{|i-j|}$ with $\rho = \exp(-\frac{\epsilon_{\text{out}}}{\epsilon_{\text{in}}} qd)$ [27, 29–33]. By using the eigenvalues and eigenvectors of the KMS matrix, we can obtain Eq. (5).

Appendix B: Wave functions of ATMG

Following [39–41], we construct the wave functions of ATMG at \bar{K} or \bar{K}' using the first-shell model, where the

momentum-space lattice consists of the nearest-neighbor shell of moiré reciprocal lattice vectors \tilde{G} under the rigid model ($w = w'$). Near \bar{K} , the term $\psi_{r,s}$ in Eq. (10) denotes the eigenfunction components of ATMG, which are constructed from the normalized eigenstates a_s of $\hat{k} \cdot \sigma_{\theta/2}$ as

$$\psi_{r,s} = \begin{cases} a_s, & r \text{ odd}, \\ t_r b_s, & r \text{ even}, \end{cases} \quad (\text{B1})$$

where $b_s = (b_{\mathbf{q}_0,s}, b_{\mathbf{q}_+,s}, b_{\mathbf{q}_-,s})^T$ is determined by $b_{\mathbf{q}_j,s} = -[v_0(\mathbf{k} + \mathbf{q}_j) \cdot \sigma_{\theta/2}]^{-1} T_j^\dagger a_s$ with $t_r = 2 \cos \phi_r$. Near \bar{K}' , the roles are exchanged, so that $\psi_{r,s} = a_s$ for even r , while $\psi_{r,s} = t_r b_s$ for odd r .

For the $N = 3$ case, using Eqs. (10) and (B1), we obtain the normalized wave functions $|\Psi_{r,s}\rangle$ near \bar{K} within the first-shell model as

$$|\Psi_{1,s}\rangle = \frac{1}{\sqrt{2 + 24\tilde{\alpha}^2}} \begin{pmatrix} a_s \\ 2b_s \\ a_s \end{pmatrix}, \quad (\text{B2a})$$

$$|\Psi_{2,s}\rangle = \frac{1}{\sqrt{2}} \begin{pmatrix} a_s \\ 0 \\ -a_s \end{pmatrix}, \quad (\text{B2b})$$

and near \bar{K}' as

$$|\Psi_{1,s}\rangle = \frac{1}{\sqrt{1 + 12\tilde{\alpha}^2}} \begin{pmatrix} b_s \\ a_s \\ b_s \end{pmatrix}. \quad (\text{B3})$$

Note that the wave functions associated with the v_1 Dirac cones at both \bar{K} and \bar{K}' exhibit symmetric behavior, whereas the wave function of $v_2 = v_0$ at \bar{K} exhibits antisymmetric behavior.

Similarly, for the $N = 4$ case, one can derive the wave functions of Dirac cones near \bar{K} as

$$|\Psi_{r,s}\rangle = \frac{2}{\sqrt{5(1 + 6t_r^2\tilde{\alpha}^2)}} \begin{pmatrix} \sin \phi_r \cdot a_s \\ \sin 2\phi_r \cdot t_r b_s \\ \sin 3\phi_r \cdot a_s \\ \sin 4\phi_r \cdot t_r b_s \end{pmatrix}, \quad (\text{B4})$$

and near \bar{K}' as

$$|\Psi_{r,s}\rangle = \frac{2}{\sqrt{5(1 + 6t_r^2\tilde{\alpha}^2)}} \begin{pmatrix} \sin \phi_r \cdot t_r b_s \\ \sin 2\phi_r \cdot a_s \\ \sin 3\phi_r \cdot t_r b_s \\ \sin 4\phi_r \cdot a_s \end{pmatrix}. \quad (\text{B5})$$

As in the $N = 3$ case, the v_1 wave functions are symmetric at both \bar{K} and \bar{K}' , in contrast to the antisymmetric nature of v_2 wave functions at both \bar{K} and \bar{K}' .

Appendix C: Calculation of the noninteracting density-density response function

We calculate the noninteracting density-density response function in the Coulomb eigenvector basis within

the first-shell model in the high-angle regime. In this limit, the velocities of the Dirac cones v_r approach v_0 since $\tilde{\alpha} = \frac{w}{2v_0 k_F \sin(\theta/2)} \ll 1$, which holds for $\theta \geq 5^\circ$. This implies that the system is effectively described by decoupled Dirac cones, corresponding to the weak-tunneling limit. Furthermore, given the block-diagonal nature of $\chi_{\alpha\beta}^{(0)} [\chi^{(0)} = \chi_{\text{odd}}^{(0)} \oplus \chi_{\text{even}}^{(0)}]$, where the block $\chi_{\text{odd(even)}}^{(0)}$ consists of elements with odd (even) indices and the correspondence of the wave functions to the one-dimensional chain model solutions, the plasmon modes are approximately determined by $1 - V_\alpha \chi_{\alpha\alpha}^{(0)} = 0$ [27]. In the following, we focus on the cases $N = 3$ and $N = 4$. Note that we only need to consider $\alpha = 1, 2$ because there are at most two Dirac cones at both the \bar{K} and \bar{K}' valleys.

In the long-wavelength limit, the in-phase mode ω_1 is determined by $1 - V_1(q) \chi_{11}^{(0)}(\mathbf{q}, \omega) = 0$. Clearly, the noninteracting response function $\chi_{11}^{(0)}$ consists of the intraband contributions of Dirac cones and is expressed as

$$\chi_{11}^{(0)}(\mathbf{q} \rightarrow 0, \omega) = \sum_{\nu, r} \frac{n_{\nu,r}}{m_r} \frac{q^2}{\omega^2} \quad (\text{C1})$$

where $m_r = k_{\text{F},r}/v_r$ and $n_{\nu,r} = gk_{\text{F},r}^2/4\pi$. Using Eqs. (5a) and (C1), we obtain the in-phase mode dispersion in Eq. (12a).

For the out-of-phase mode ω_2 , we obtain the noninteracting response function $\chi_{22}^{(0)}$. Since the plasmon dispersion is determined by $1 - V_2 \chi_{22}^{(0)} = 0$, the plasmon mode requires $\chi_{22}^{(0)}(q, \omega)$ to be real and positive. Consequently, we restrict our analysis to the region outside the particle-hole continuum and exclude regimes where $\text{Re}[\chi_{22}^{(0)}] < 0$. The response function in the zero-momentum limit is governed solely by interband transitions between $|\Psi_{1,s}\rangle$ and $|\Psi_{2,s}\rangle$, given by

$$\begin{aligned} \chi_{22}^{(0)}(q \rightarrow 0, \omega) &= g \sum_{\nu, ss', r \neq r'} \int \frac{d^2 k}{(2\pi)^2} \frac{f_{\mathbf{k},r,s} - f_{\mathbf{k},r',s'}}{\omega + (sv_r - s'v_{r'})k} \\ &\times |\langle \Psi_{r,s} | U_2 | \Psi_{r',s'} \rangle|^2 \\ &= gF_N \int_{k_{\text{F},2}}^{k_{\text{F},1}} \frac{k dk}{2\pi} \left[\frac{1}{\omega - v_{21}k} - \frac{1}{\omega + v_{21}k} \right] \\ &= gF_N \frac{\omega}{2\pi v_{21}^2} \left[2 \frac{v_{21}}{\omega} (k_{\text{F},2} - k_{\text{F},1}) \right. \\ &\left. + \ln \frac{(\omega + v_{21}k_{\text{F},1})(\omega - v_{21}k_{\text{F},2})}{(\omega - v_{21}k_{\text{F},1})(\omega + v_{21}k_{\text{F},2})} \right]. \end{aligned} \quad (\text{C2})$$

which is valid for $\omega > v_{21}k_{\text{F},1}$. Here, we used $|\Psi_{1,s}\rangle$ and $|\Psi_{2,s}\rangle$ obtained in Appendix B, and F_N represents the overlap factor with the antisymmetric oscillation matrix U_2 . To demonstrate that the intraband contribution to $\chi_{22}^{(0)}$ vanishes, we evaluate the element $\langle \Psi_{r,s} | U_2 | \Psi_{r,s} \rangle$. For the $N = 3$ case, it is straightforward to see that this element is zero. Note that, unlike in the $N = 3$ case, this term does not vanish at each valley for $N = 4$; instead, the contributions from \bar{K} and \bar{K}' mutually cancel. In the

zero-momentum limit, the equation $1 - V_2(\mathbf{q})\chi_{22}^{(0)}(\mathbf{q}, \omega) = 0$ reduces to the following expression for the out-of-phase plasmon gap:

$$\omega = v_{21}k_{F,1} + \delta\omega_2^{(N)} \quad (\text{C3})$$

where

$$\delta\omega_2^{(N)} = \frac{(\omega + v_{21}k_{F,1})(\omega - v_{21}k_{F,2})}{\omega + v_{21}k_{F,2}} \times \exp\left[\frac{v_{21}}{\omega}\left\{2(k_{F,2} - k_{F,1}) - \frac{v_{21}\varepsilon_{\text{in}}(1 - \cos(\frac{\pi}{N}))}{F_N e^2 g d}\right\}\right]. \quad (\text{C4})$$

Clearly, $\delta\omega_2^{(N)} \rightarrow 0$ when $\frac{e^2}{v_{21}\varepsilon_{\text{in}}} \rightarrow 0$, meaning that the out-of-phase plasmon gap becomes $\omega_{\text{gap},2} = v_{21}k_{F,1}$ in the weak Coulomb-interaction limit. Note that while Eq. (C2) presents several interband transitions between the v_2 and v_1 Dirac cones, the dominant contribution among the nonvanishing terms arises from the transition associated with $v_{21}k_{F,1}$.

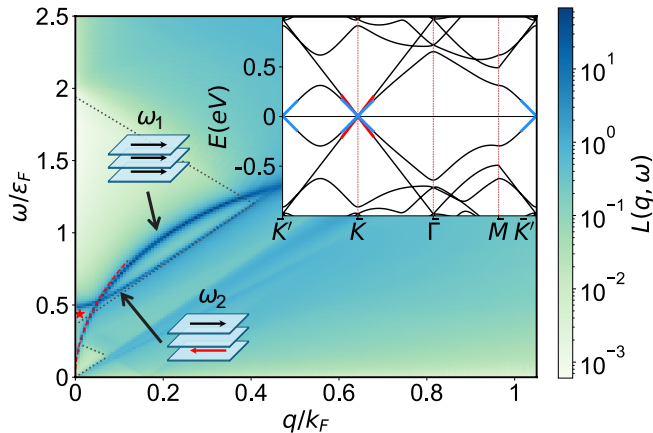


FIG. 8. Loss function $L(\mathbf{q}, \omega)$ of an unbiased AT3G system at a twist angle $\theta = 5^\circ$ with $\varepsilon_F = 0.2$ eV ($n_{\text{tot}} = 1.3 \times 10^{13}$ cm $^{-2}$). Here, \mathbf{q} is chosen along the $\bar{\Gamma} - \bar{K}$ direction.

The analysis presented above for $N = 3$ and $N = 4$ can be generalized to higher N systems. In the presence of multiple Dirac cones, the dominant contribution in $\chi_{\alpha\alpha}^{(0)}$ arises from transitions between Dirac cones whose indices differ by $\alpha - 1$ [27]. Since the high-angle regime corresponds to the weak tunneling limit, the several interband transitions for the out-of-phase mode ω_α can be approximately replaced by the transitions between the

v_α and v_1 Dirac cones, analogous to the isotropic tunneling case [27]. This implies that the out-of-phase mode is described by Eq. (13) in the weak Coulomb-interaction regime.

Appendix D: Directional dependence of plasmon dispersion on momentum transfer q

We presented the plasmon dispersion along the $\bar{\Gamma} - \bar{M}$ direction in the main text, given that the low-energy Hamiltonian is effectively isotropic near the Dirac points. While the numerical band structure is anisotropic, this directional dependence becomes negligible for the long-wavelength behavior. Figure 8 shows the loss function along the $\bar{\Gamma} - \bar{K}$ direction. This is consistent with that along the $\bar{\Gamma} - \bar{M}$ direction, confirming the isotropic character of the plasmon modes in the long-wavelength limit.

Appendix E: Electronic structure of biased ATMG

Following the perturbation theory of Shin *et al.* [41], we consider the Hamiltonian for $N = 3$ in the presence of the interlayer potential difference U . At \bar{K} , we calculate the perturbation matrix in the basis of the wave functions given in Eq. (B2) with $H_U = \text{diag}[-U\mathbb{I}_2, \mathbf{0}_6, U\mathbb{I}_2]$. The 2×2 perturbation matrix elements are $[H_U]_{11} = [H_U]_{22} = 0$ and $[H_U]_{12} = [H_U]_{21} = -U/\sqrt{1 + 12\tilde{\alpha}^2}$, and the effective Hamiltonian for $N = 3$ in Eq. (17) is derived by diagonalizing the following matrix

$$H_{\bar{K}} = \begin{bmatrix} v_1(\mathbf{k} \cdot \boldsymbol{\sigma}) & -C(\tilde{\alpha})U \\ -C(\tilde{\alpha})U & v_2(\mathbf{k} \cdot \boldsymbol{\sigma}) \end{bmatrix}, \quad (\text{E1})$$

where $C(\tilde{\alpha}) = 1/\sqrt{1 + 12\tilde{\alpha}^2}$, assuming the regime $v_{21}k \ll U$ near \bar{K} . Note that the perturbed wave functions become linear combinations of $|\Psi_{1,s}\rangle$ and $|\Psi_{2,s}\rangle$. This mixing generates non-contributing components with vanishing elements ($\langle \Psi_{r,s} | U_2 | \Psi_{r,s} \rangle = 0$) into the interband transitions between Dirac cones, leading to a reduction in the overlap factor F_N . Consequently, the Coulomb-interaction-induced shift of the plasmon gap is suppressed.

In contrast, at \bar{K}' , only a single Dirac cone with velocity v_1 exists, described by the wave function in Eq. (B3). Consequently, the perturbation matrix vanishes, leaving the Dirac cone at \bar{K}' unaltered to leading order in U . This implies that the out-of-phase mode ω_2 is solely determined by the interband transitions at \bar{K} , with no contribution from the \bar{K}' valley.

[1] Y. Cao, V. Fatemi, A. Demir, S. Fang, S. L. Tomarken, J. Y. Luo, J. D. Sanchez-Yamagishi, K. Watanabe, T. Taniguchi, E. Kaxiras, R. C. Ashoori, and P. Jarillo-

Herrero, Correlated insulator behaviour at half-filling in magic-angle graphene superlattices, *Nature (London)* **556**, 80 (2018).

[2] Y. Cao, V. Fatemi, S. Fang, K. Watanabe, T. Taniguchi, E. Kaxiras, and P. Jarillo-Herrero, Unconventional superconductivity in magic-angle graphene superlattices, *Nature (London)* **556**, 43 (2018).

[3] M. Yankowitz, S. Chen, H. Polshyn, Y. Zhang, K. Watanabe, T. Taniguchi, D. Graf, A. F. Young, and C. R. Dean, Tuning superconductivity in twisted bilayer graphene, *Science* **363**, 1059 (2019).

[4] X. Lu, P. Stepanov, W. Yang, M. Xie, M. A. Aamir, I. Das, C. Urgell, K. Watanabe, T. Taniguchi, G. Zhang, A. Bachtold, A. H. MacDonald, and D. K. Efetov, Superconductors, orbital magnets and correlated states in magic-angle bilayer graphene, *Nature (London)* **574**, 653 (2019).

[5] J. M. B. Lopes dos Santos, N. M. R. Peres, and A. H. Castro Neto, Graphene bilayer with a twist: Electronic structure, *Phys. Rev. Lett.* **99**, 256802 (2007).

[6] S. Shallcross, S. Sharma, and O. A. Pankratov, Quantum interference at the twist boundary in graphene, *Phys. Rev. Lett.* **101**, 056803 (2008).

[7] E. J. Mele, Commensuration and interlayer coherence in twisted bilayer graphene, *Phys. Rev. B* **81**, 161405(R) (2010).

[8] G. Li, A. Luican, J. M. B. Lopes dos Santos, A. H. Castro Neto, A. Reina, J. Kong, and E. Y. Andrei, Observation of Van Hove singularities in twisted graphene layers, *Nat. Phys.* **6**, 109 (2010).

[9] S. Shallcross, S. Sharma, E. Kandelaki, and O. A. Pankratov, Electronic structure of turbostratic graphene, *Phys. Rev. B* **81**, 165105 (2010).

[10] R. Bistritzer and A. H. MacDonald, Transport between twisted graphene layers, *Phys. Rev. B* **81**, 245412 (2010).

[11] J. M. B. Lopes dos Santos, N. M. R. Peres, and A. H. Castro Neto, Continuum model of the twisted graphene bilayer, *Phys. Rev. B* **86**, 155449 (2012).

[12] G. Trambly de Laissardière, D. Mayou, and L. Magaud, Localization of Dirac electrons in rotated graphene bilayers, *Nano Lett.* **10**, 804 (2010).

[13] E. Suárez Morell, J. D. Correa, P. Vargas, M. Pacheco, and Z. Barticevic, Flat bands in slightly twisted bilayer graphene: Tight-binding calculations, *Phys. Rev. B* **82**, 121407(R) (2010).

[14] R. Bistritzer and A. H. MacDonald, Moiré bands in twisted double-layer graphene, *Proc. Natl. Acad. Sci. USA* **108**, 12233 (2011).

[15] G. Tarnopolsky, A. J. Kruchkov, and A. Vishwanath, Origin of magic angles in twisted bilayer graphene, *Phys. Rev. Lett.* **122**, 106405 (2019).

[16] T. Stauber, P. San-Jose, and L. Brey, Optical conductivity, Drude weight and plasmons in twisted graphene bilayers, *New J. Phys.* **15**, 113050 (2013).

[17] T. Stauber and H. Kohler, Quasi-flat plasmonic bands in twisted bilayer graphene, *Nano Lett.* **16**, 6844 (2016).

[18] C. Lewandowski and L. Levitov, Intrinsically undamped plasmon modes in narrow electron bands, *Proc. Natl. Acad. Sci. USA* **116**, 20869 (2019).

[19] P. Novelli, I. Torre, F. H. L. Koppens, F. Taddei, and M. Polini, Optical and plasmonic properties of twisted bilayer graphene: Impact of interlayer tunneling asymmetry and ground-state charge inhomogeneity, *Phys. Rev. B* **102**, 125403 (2020).

[20] T. Stauber, T. Low, and G. Gómez-Santos, Chiral response of twisted bilayer graphene, *Phys. Rev. Lett.* **120**, 046801 (2018).

[21] N. C. H. Hesp, I. Torre, D. Rodan-Legrain, P. Novelli, Y. Cao, S. Carr, S. Fang, P. Stepanov, D. Barcons-Ruiz, H. H. Sheinfux, *et al.*, Observation of interband collective excitations in twisted bilayer graphene, *Nature Physics* **17**, 1162 (2021).

[22] T. Huang, X. Tu, C. Shen, B. Zheng, J. Wang, H. Wang, K. Khaliji, S. H. Park, Z. Liu, T. Yang, *et al.*, Observation of chiral and slow plasmons in twisted bilayer graphene, *Nature* **605**, 63 (2022).

[23] L. Cavicchi, I. Torre, P. Jarillo-Herrero, F. H. L. Koppens, and M. Polini, Theory of intrinsic acoustic plasmons in twisted bilayer graphene, *Phys. Rev. B* **110**, 045431 (2024).

[24] J.-J. Zhu, S. M. Badalyan, and F. M. Peeters, Plasmonic excitations in Coulomb-coupled N -layer graphene structures, *Phys. Rev. B* **87**, 085401 (2013).

[25] P. D. T. Kim and M. Nguyen Van, Plasmon modes in N -layer graphene structures at zero temperature, *J. Low Temp. Phys.* **201**, 311 (2020).

[26] N. Van Men, Plasmon modes in N -layer silicene structures, *J. Phys. Condens. Matter* **34**, 085301 (2021).

[27] T. Kim, E. H. Hwang, and H. Min, Plasmons in N -layer systems, *Phys. Rev. B* **112**, L041111 (2025).

[28] S. Das Sarma and E. H. Hwang, Plasmons in coupled bilayer structures, *Phys. Rev. Lett.* **81**, 4216 (1998).

[29] M. Kac, W. Murdock, and G. Szegő, On the eigenvalues of certain Hermitian forms, *Indiana Univ. Math. J.* **2**, 767 (1953).

[30] W. F. Trench, Properties of some generalizations of Kac-Murdock-Szegő matrices, in *Structured Matrices in Mathematics, Computer Science, and Engineering II*, edited by V. Olshevsky (American Mathematical Society, Providence, RI, 2001), *Contemp. Math.* **281**, pp. 233–245.

[31] J. M. Bogoya, A. Böttcher, S. M. Grudsky, and E. A. Maximenko, Eigenvectors of Hermitian Toeplitz matrices with smooth simple-loop symbols, *Lin. Alg. Appl.* **493**, 606 (2016).

[32] G. Fikioris, Spectral properties of Kac-Murdock-Szegő matrices with a complex parameter, *Lin. Alg. Appl.* **553**, 182 (2018).

[33] O. Narayan and B. S. Shastry, Generalized Toeplitz-Hankel matrices and their application to a layered electron gas, *J. Phys. A* **54**, 175201 (2021).

[34] D. Pines and P. Nozieres, *The Theory of Quantum Liquids* (Benjamin, New York, 1966).

[35] G. D. Mahan, *Many-particle Physics*, 3rd ed. (Springer, New York, 2000).

[36] G. F. Giuliani and G. Vignale, *Quantum Theory of the Electron Liquid* (Cambridge University Press, Cambridge, 2005).

[37] T. Kamatani, S. Kitamura1, N. Tsuji, R. Shimano, and T. Morimoto, Optical response of the Leggett mode in multiband superconductors in the linear response regime, *Phys. Rev. B* **105**, 094520 (2022).

[38] R. E. V. Profumo, M. Polini, R. Asgari, R. Fazio, and A. H. MacDonald, Electron-electron interactions in decoupled graphene layers, *Phys. Rev. B* **82**, 085443 (2010).

[39] E. Khalaf, A. J. Kruchkov, G. Tarnopolsky, and A. Vishwanath, Magic angle hierarchy in twisted graphene multilayers, *Phys. Rev. B* **100**, 085109 (2019).

[40] N. Leconte, Y. Park, J. An, A. Samudrala, and J. Jung, Electronic structure of lattice relaxed alternating twist tNG multilayer graphene: From few layers to bulk AT-graphite, *2D Mater.* **9**, 044002 (2022).

- [41] K. Shin, Y. Jang, J. Shin, J. Jung, and H. Min, Electronic structure of biased alternating-twist multilayer graphene, *Phys. Rev. B* **107**, 245139 (2023).
- [42] J. Jung, A. Raoux, Z. Qiao, and A. H. MacDonald, Ab initio theory of moiré superlattice bands in layered two-dimensional materials, *Phys. Rev. B* **89**, 205414 (2014).
- [43] K. Uchida, S. Furuya, J.-I. Iwata, and A. Oshiyama, Atomic corrugation and electron localization due to moiré patterns in twisted bilayer graphenes, *Phys. Rev. B* **90**, 155451 (2014).
- [44] M. M. van Wijk, A. Schuring, M. I. Katsnelson, and A. Fasolino, Relaxation of moiré patterns for slightly misaligned identical lattices: Graphene on graphite, 2D Mater. **2**, 034010 (2015).
- [45] N. R. Chebrolu, B. L. Chittari, and J. Jung, Flat bands in twisted double bilayer graphene, *Phys. Rev. B* **99**, 235417 (2019).
- [46] G. Borghi, M. Polini, R. Asgari, and A. H. MacDonald, Dynamical response functions and collective modes of bilayer graphene, *Phys. Rev. B* **80**, 241402(R) (2009).
- [47] C.-Y. Lin, C.-H. Ho, J.-Y. Wu, and M.-F. Lin, Unusual electronic excitations in aba trilayer graphene, *Sci. Rep.* **10**, 11106 (2020).
- [48] Y. Mohammadi, Tunable plasmon modes in doped AA-stacked bilayer graphene, *Superlattices Microstruct.* **156**, 106935 (2021).